Accepted Manuscript

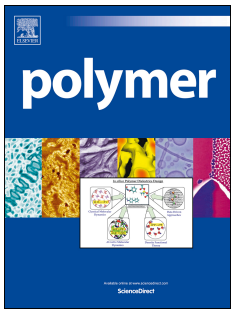

Investigation of the micro- and nano-scale architecture of cellulose hydrogels with plant cell wall polysaccharides: A combined USANS/SANS study

Marta Martínez-Sanz, Deirdre Mikkelsen, Bernadine M. Flanagan, Christine Rehm, Liliana de Campo, Michael J. Gidley, Elliot P. Gilbert

PII: S0032-3861(16)30570-5

DOI: 10.1016/j.polymer.2016.07.015

Reference: JPOL 18821

To appear in: *Polymer*

Received Date: 28 April 2016

Accepted Date: 3 July 2016

Please cite this article as: Martínez-Sanz M, Mikkelsen D, Flanagan BM, Rehm C, de Campo L, Gidley MJ, Gilbert EP, Investigation of the micro- and nano-scale architecture of cellulose hydrogels with plant cell wall polysaccharides: A combined USANS/SANS study, *Polymer* (2016), doi: 10.1016/j.polymer.2016.07.015.

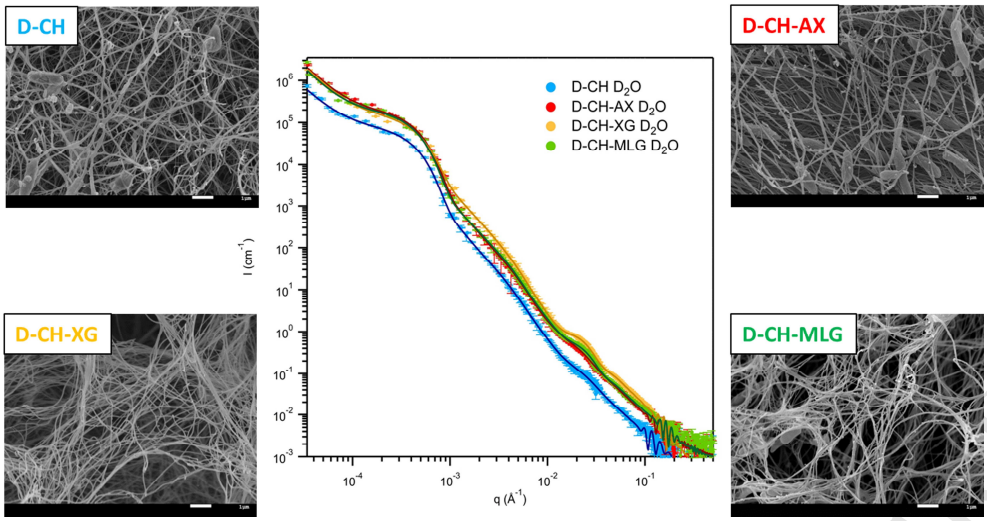

INVESTIGATION OF THE MICRO- AND NANO-SCALE ARCHITECTURE OF CELLULOSE HYDROGELS WITH PLANT CELL WALL POLYSACCHARIDES: A COMBINED USANS/SANS STUDY

Marta Martínez-Sanz [a,b], Deirdre Mikkelsen [b], Bernadine M. Flanagan [b], Christine Rehm [a], Liliana de Campo [a], Michael J. Gidley [b] and Elliot P. Gilbert [a*]

[a] Bragg Institute, Australian Nuclear Science and Technology Organisation, Locked Bag 2001, Kirrawee DC, NSW 2232 (Australia).

[b] ARC Centre of Excellence in Plant Cell Walls, Centre for Nutrition and Food Sciences, Queensland Alliance for Agriculture and Food Innovation, The University of Queensland, St. Lucia, Brisbane, QLD 4072 (Australia).

*Corresponding author: Tel.: +61 297179470; fax: +61 297173606

E-mail address: elliot.gilbert@ansto.gov.au

Abstract

The structure of protiated, deuterated and composite cellulose hydrogels with plant cell wall (PCW) polysaccharides has been investigated by combined USANS/SANS experiments, complemented with spectroscopy and microscopy. The broad size range covered by the USANS/SANS experiments enabled the identification of cellulose architectural features in the cross-sectional and longitudinal directions. In the cross-sectional direction, cellulose ribbons are modelled as core-shell structures. Xyloglucan and mixed linkage glucans interfere with the cellulose crystallization process, reducing the crystallinity and establishing cross-bridges between ribbons. However, only xyloglucan is able to establish strong interactions with the cellulose microfibrils, affecting the properties of the ribbons' core. Longitudinally, the ribbons are hypothesised to present a ca. 1.4-1.5 μm periodic twist with a crystallite length of ca. 140-180 nm for the individual microfibrils. These results highlight the potential of USANS/SANS techniques to investigate the multi-scale architecture of cellulose hydrogels as well as the interaction mechanism between cellulose and PCW polysaccharides.

Keywords: small angle scattering; neutron scattering; deuteration; cellulose; hydrogels; *Komagataeibacter xylinus*

1. Introduction

Cellulose hydrogels are highly hydrated systems in which cellulose fibrillar networks interact with interstitial water at different structural levels. Several bacterial species such as *Komagataeibacter xylinus* (formerly known as *Gluconacetobacter xylinus*), are able to synthesise cellulose hydrogels in the form of pellicles when inoculated into a culture medium rich in carbohydrates or polyols [1]. The synthesised cellulose hydrogels present a high degree of purity and hydration (ca. 99 wt.% H_2O) and possess a complex structure in which cellulose is hierarchically assembled to form different structural features [2, 3]. Cellulose chains, consisting of glucose units connected by β-1-4-linkages, are typically arranged into larger structures known as cellulose microfibrils. These microfibrils contain distinct domains with differing levels of cellulose chain ordering: (i) crystalline (i.e. highly ordered chains), (ii) paracrystalline (i.e. regions with loose molecular packing or some degree of crystal distortion) and (iii) amorphous (i.e. regions with randomly arranged cellulose chains) domains. At the same time, the presence of hydroxyl groups on the surface of the microfibrils leads to the creation of cellulose-cellulose and cellulose-water interactions by means of a strong hydrogen bonded network, resulting in the formation of structures which, in the particular case of bacterial cellulose, are known as cellulose ribbons.

Cellulose hydrogels are attracting a great deal of interest across diverse research areas, since they present remarkable properties for their application in the fields of biomedicine [4-6], the food industry [7] and polymeric bionanocomposites [8-11], as well as having been shown to serve as excellent model systems to investigate the structure and interaction mechanisms of cellulose with other components found in plant cell walls (PCWs) [12-18]. PCWs are complex systems in which cellulose microfibrils, the main

load-bearing component, are embedded in an amorphous matrix of polysaccharides and glycoproteins. The matrix composition and interconnection between the different components is specific to each type of PCW and determine the properties of the respective plant tissue. Xyloglucan (XG) and pectins are the major non-cellulosic polysaccharides found in the primary cell walls from dicotyledonous plants and non-commelinoid monocotyledonous plants, known as Type I walls. On the other hand, arabinoxylans (AX) and (1→3)(1→4)-β-D-glucans, i.e. mixed linkage glucans (MLG), constitute the predominant matrix polysaccharides in type II walls, which are found in commelinoid monocotyledons, including cereals and grasses [19]. Understanding the interaction mechanism of cellulose with these PCW polysaccharides would therefore provide substantial insights into their biosynthetic and structural roles, enabling connections to be established between the specific requirements of different PCW types and both their composition and structure.

Investigation of the PCW structure is, however, extremely complicated due to several inherent difficulties. For example, the ability of plants to adapt to modifications in their cell wall composition [20] has precluded the drawing of definitive conclusions on the role of different PCW polysaccharides. Furthermore, it is unclear how the chemical or enzymatic processes that are typically applied to sequentially extract PCW components – essentially a deconstructionist approach - affect the cellulose network. As an alternative, the synthesis of composite cellulose hydrogels through the incorporation of PCW components into the bacterial culture medium constitutes a very promising approach, as it offers the possibility of studying the effect of selected PCW polysaccharides on the cellulose biosynthesis process and on the properties of the synthesised hydrogels, without the interference of additional components. The incorporation of several PCW

polysaccharides such as XG, mannans, AX, MLG and pectins using this approach is well reported in the literature [2, 12, 13, 15-18, 21-27]. From some of these studies it has been inferred that only XG and mannans are able to interfere with the cellulose crystallisation process, reducing the crystallinity index and promoting the formation of the cellulose I_β allomorph [14, 15, 17, 18, 23, 26]. This indicates that a certain fraction of XG (or mannan) is able to interact directly with the individual cellulose microfibrils. In addition, a different fraction of XG, which interacts with the surface of cellulose ribbons, has been identified [14, 15, 17]. This fraction is thought to correspond to the thin XG cross-bridges detected in the microscopy images from composite hydrogels [14, 15, 17, 26]. In contrast to XG, neither AX nor MLG have been reported to affect the crystalline arrangement of cellulose and they have been suggested to interact with cellulose ribbons via a surface adsorption mechanism [15, 16, 23].

It is evident that in the case of highly hydrated systems such as cellulose hydrogels, any drying process should be avoided as it may induce strong structural alterations. In this sense, small angle X-ray and neutron scattering techniques (SAXS and SANS) represent a clear advantage over the typically used microscopy characterisation techniques, since they enable the characterisation of native cellulose hydrogels, covering a size range from 1 nm to several hundreds of nm, with minimal sample preparation [28]. Moreover, in the particular case of SANS, the different scattering length of hydrogen and deuterium opens up the possibility of enhancing the scattering length density (SLD) contrast by means of selective deuterium labelling. Successful production of deuterated bacterial cellulose by utilising deuterated glycerol [29, 30] and glucose [3, 31] as the carbon sources has been recently reported. Moreover, the similarity in the multi-scale assembly (from the molecular to the nano-scale size range) of protiated and analogous deuterated cellulose

hydrogels has been demonstrated by the combination of SAXS and SANS with complementary microscopy, spectroscopy and diffraction methods [3]. In spite of the aforementioned, the great potential of these techniques can only be fully exploited if a suitable model, based on prior knowledge of the system, is utilised to interpret the data. It has been recently demonstrated that the conventional models which consider cellulose ribbons as one-phase objects surrounded by bulk solvent are not appropriate[2]. Instead, a core-shell model accounting for the different structural levels and cellulose-water interactions has been proven to satisfactorily describe the nano-architecture of native cellulose hydrogels [2, 3]. However, the size range covered by small angle scattering techniques does not allow the identification of structural features relevant to the cellulose assembly in the ribbon longitudinal direction. Moreover, the values reported in the literature for the length of bacterial cellulose crystalline domains, ranging from 100 nm up to several micrometres [32-37], are merely based on microscopy characterisation of samples extracted by means of enzymatic or acid digestion. The large variability in the reported lengths is related to the heterogeneity of the applied acid hydrolysis procedures. It is known that several factors such as acid concentration, temperature and hydrolysis time may strongly affect the extent to which the amorphous and crystalline domains are digested [34, 36] and, therefore, varying any of these parameters is expected to affect the morphology of the extracted material. In this context, ultra-small angle scattering techniques, which are able to cover size ranges up to ca. 10 μm, represent an excellent approach to provide a complete picture of the cellulose multi-scale structure in native cellulose hydrogels when combined with small angle scattering techniques.

In the present work, we report on the multi-scale characterisation of pure protiated and partially deuterated cellulose hydrogels, as well as associated composites of cellulose with

three different PCW polysaccharides through a combined USANS/SANS study, complemented by spectroscopy and microscopy techniques. By extending the size range up to the micron scale, structural features characteristic of the longitudinal structure of cellulose can be identified. Through the strategic combination of the multi-length scale techniques selected, the effect of PCW polysaccharides on the architecture of the synthesised hydrogels has been investigated and related to their structural roles.

2. Materials and methods

2.1 Production of pure cellulose and composite hydrogels

Protiated and deuterated cellulose, as well as associated composite PCW hydrogels were prepared as described by Martínez-Sanz *et al.* [3], with the following exceptions. Briefly, *Komagataeibacter xylinus* (formerly *Gluconacetobacter xylinus)* strain ATCC 53524 (American Type Culture Collection, Manassas, VA, USA) was cultivated in Hestrin Schramm (HS) medium [38] at pH 5.0, containing 2.0% (w/v) glucose or deuterated glucose (552003-1G – Sigma- Aldrich, Castle Hill, NSW, Australia) as the sole carbon sources to generate the protiated (H-CH) and the deuterated cellulose hydrogels (D-CH), as well as the composite hydrogels incorporating PCW polysaccharides (D-CH-AX, D-CH-XG and D-CH-MLG). The latter materials were produced as described by Mikkelsen and co-workers [16, 39], by adding to this medium, as desired, 0.5% (w/v) medium viscosity (22 cSt) wheat AX (lot 40302b), medium viscosity (28 cSt) barley MLG (lot 90802), or tamarind seed XG (lot 100403), supplied by Megazyme International Ireland (County Wicklow, Ireland). Incubations were performed at 30 °C for 48 h under static conditions. The materials were subsequently harvested and washed for 90 min in ice-cold sterile milliQ water, under gentle agitation (150 rpm), with a total of five rinses (until white in appearance) to remove excess medium and polymers non-specifically trapped within the

cellulose mat, and to dislodge loosely-associated bacterial cells. Thereafter, all samples were stored in 0.02% (w/v) sodium azide solution at 4°C, until used for experiments.

The wet weights of all samples were recorded using an analytical balance at room temperature and the densities were calculated by dividing the wet weights by the average volume of the hydrated hydrogel (calculated using the dimensions of the growth vessel and the thickness of the hydrated hydrogel, measured using digital calipers).

2.2 Compositional Analysis

2.2.1. Monosaccharide analysis

The amount AX and XG incorporated into the D-CH-AX and D-CH-XG composite hydrogels was calculated from individual monosaccharide contents of the dry samples using the method by Pettolino et al. [40]. Briefly, the air-dried samples (1-5 mg) were cut with a scalpel, hydrolysed with sulphuric acid, reduced and acetylated. The alditol acetates of the monosaccharides were subsequently identified and quantified by gas chromatography-mass spectrometry (GC-MS).

2.2.2 β–glucan colorimetric assay

The amount of MLG in the D-CH-MLG composite hydrogel was assessed using the mixed-linkage β-D-glucan assay kit (Megazyme International Ireland Ltd, County Wicklow, Ireland), according to the manufacturer's protocol.

2.3 Scanning electron microscopy (SEM)

The microarchitectures of the fully hydrated H-CH, D-CH, as well as composite D-CH hydrogels were visualised by appropriately preparing samples of approximately 1cm^2 for

field emission SEM (FESEM) as previously described by Martínez-Sanz *et al.* [3]. Images were obtained using a JSM 7100F electron microscope (JEOL, Tokyo, Japan) with an accelerating voltage of 5 kV and a working distance of 10 mm. Cross-sections of cellulose ribbons were determined using ImageJ software [41] from the FESEM micrographs at their original magnification.

2.4 Small angle neutron scattering (SANS)

SANS measurements were performed on the 40 m QUOKKA instrument at the OPAL reactor [42]. Four configurations were used to cover a q range of ca. 0.0006-0.6 $Å^{-1}$ where q is the magnitude of the scattering vector defined as $q = \frac{4\pi}{\lambda}\sin\theta$, λ is the wavelength in Å and 2θ is the scattering angle. These configurations were: (i) source-to-sample distance (SSD) = 20.2 m with focusing optics using MgF_2 lenses; (ii) SSD = 20.2 m, sample-to-detector distance (SDD) = 20.1 m; (iii) SSD = 3.9 m, SSD = 4.0 m and (iv) SSD = 10.0 m, SDD = 1.3 m, with 10% wavelength resolution and λ = 8.1 Å for (i) and λ = 5.0 Å for (ii)-(iv). The source and sample aperture diameters were 50 mm and 12.5 mm, respectively. Native H-CH, D-CH and composite D-CH hydrogels were studied by placing the samples in 1 mm path length cells with demountable quartz windows and filling the cells with D_2O. To maximize D/H exchange, prior to the SANS measurements, the hydrogels were soaked in D_2O with an approximate sample/solvent ratio of 1g/30mL. The hydrogels were initially soaked for 24h and, subsequently, an additional exchange step with fresh solvent was carried out for at least a further 24h. The demountable cells used for these SANS experiments have been designed for USANS and enable beam dimensions of up to 5 x 5 cm^2.

SANS data were reduced using NCNR SANS reduction macros [43] modified for the QUOKKA instrument, using the Igor software package (Wavemetrics, Lake Oswego, OR) with data corrected for empty cell scattering, transmission, and detector response and transformed onto an absolute scale by the use of an attenuated direct beam transmission measurement.

2.5 Ultra-Small angle neutron scattering (USANS)

USANS experiments were performed on identical samples to SANS, using the KOOKABURRA instrument at the OPAL reactor [44]. KOOKABURRA is based on the Bonse–Hart technique using two sets of identical, 5-bounce, channel-cut, perfect Si single crystals, the "monochromator" and "analyser" respectively, arranged in non-dispersive parallel geometry in Bragg reflection. Using a neutron wavelength of 4.74 Å and a Cd aperture with a diameter of 35 mm, a *q*-range of ca. 0.00003–0.007 $Å^{-1}$ was accessed. Rocking curve profiles were measured by rotating the analyser crystal away from the aligned peak position (the position in which the undeviated neutrons are reflected onto the detector) and measuring the neutron intensity as a function of *q*. The USANS data were reduced with an empty cell as background and converted onto an absolute scale using adapted python scripts based on the NCNR USANS reduction macros[43]. The reduced slit-smeared data were desmeared using the Lake algorithm [43] before merging with the SANS data.

2.6 Data fitting

The reduced SANS and USANS data were merged, obtaining intensity versus q plots with a q range of ca. 3×10^{-5} – 0.6 $Å^{-1}$. As an example, Figure 1 shows the q ranges covered by the four different SANS configurations (three conventional and one focussing) as well as

by the USANS experiment. The background contribution for each sample was estimated by calculating the slope of the linear region at high q on an $I \cdot q^4$ versus q^4 plot (Porod plot). The value of the slope obtained was used to determine the level of constant background (bulk D_2O and incoherent scattering from the protonated material) which was subsequently subtracted from each sample. All the scattering plots presented in this work have been background subtracted by following this procedure.

The function utilised to fit the experimental data over the extremely broad q range available comprises the sum of a three-level Beaucage model (to account for the structural features contained within the region $3 \times 10^{-5} < q / Å^{-1} < 6 \times 10^{-3}$) plus a core-shell cylinder model (to describe the shoulder features within the region $0.01 < q / Å^{-1} < 0.10$). The resulting sum function is as follows:

$$I(q) = \left[\sum_{i=1}^{i=3} G_i \exp\left(-q^2 \cdot \frac{R_{g,i}^2}{3}\right) + \frac{B_i \left[\mathrm{erf}\left(\frac{qR_{g,i}}{\sqrt{6}}\right)\right]^{3P_i}}{q^{P_i}}\right]$$

$$+ \left[\frac{sf}{V_{shell}} \cdot \sum_{R_{shell}} n(R_{core}, \sigma_{core}) \cdot P(q, R_{core}, R_{shell}, L, SLD_{core}, SLD_{shell}, SLD_{solv})\right] + bkg \quad (1)$$

where the first term contained within brackets corresponds to the three-level Beaucage model, the second term corresponds to the core-shell cylinder model and the third term accounts for the incoherent background remaining after solvent background subtraction (which in this case was close to zero, as it had already been subtracted using the Porod plot described above).

The Beaucage model considers that, for each individual level, the scattering intensity is the sum of a Guinier term and a power-law function [45, 46]. In the first term from equation

(1) $G_i = c_i V_i \Delta SLD_i^2$ is the exponential prefactor (where V_i is the volume of the particle and ΔSLD_i is the SLD contrast existing between the ith structural feature and the surrounding solvent), $R_{g,i}$ is the radius of gyration describing the average size of the ith level structural feature and B_i is a q-independent prefactor specific to the type of power-law scattering with power-law exponent, P_i. In this particular case, the largest sized structural level (i.e. level 1) could be described by a simple power-law function (with the first term in the Beaucage model equation equal to zero).

The core-shell cylinder model, corresponding to the second term in equation (1), is a slightly modified version of the core-shell model described in a previous work [2], which accounts for a cylinder structure with polydisperse core and fixed thickness shell (no power-law term was included in this case, as this is already being accounted for by the Beaucage model). A detailed description of the form factor function and the parameters defining the core-shell model can be found elsewhere [2]. In this particular case, the scale factor was allowed to vary between 0.002 and 0.05 during the fitting process. This range was based on uncertainties concerning the sample thickness (0.8-1.0 mm), knowledge of the dry weight (0.5-2.0%) and errors in the measurements thereof. The SLD values of the native hydrogels (i.e. in 100% H_2O) were estimated by assuming an initial molecular structure of $C_6H_{10}O_5$ for H-CH and $C_6H_5D_5O_5$ for D-CH. As described below, the deuteration degree for D-CH is based on the FT-IR analysis and is consistent with the value previously reported for a D-CH sample prepared by following exactly the same procedure [3]. The cellulose crystallinity values, calculated from the ^{13}C-NMR experiments, were also considered in the calculations by re-calculating the physical density of cellulose as:

$$\rho_{cellulose} = \left[X_C \cdot \rho_{crystalline\ cellulose}\right] + \left[(1 - X_C) \cdot \rho_{amorphous\ cellulose}\right].$$

2.7 ^{13}C CP/MAS Nuclear Magnetic Resonance (NMR) spectroscopy

The solid-state ^{13}C CP/MAS NMR experiments were performed at a ^{13}C frequency of 75.46 MHz on a Bruker MSL-300 spectrometer. One hydrogel specimen, squeeze dried to ~90% water, was packed in a 4-mm diameter, cylindrical, PSZ (partially-stabilized zirconium oxide) rotor with a perfluorinated polymer (KelF) end cap. Due to the limited amount of sample, it was necessary to pack the rotor with Teflon tape so the material was placed in the middle of the rotor to maximize signal intensity. The rotor was spun at 5-6 kHz at the magic angle (54.7^{o}). The 90^{o} pulse width was 5 μs and a contact time of 1 ms was used for all samples with a recycle delay of 3 s. The spectral width was 38 kHz, acquisition time 50 ms, time domain points 2000, transform size 4000 and line broadening 50 Hz. At least 20,000 scans were accumulated for each spectrum. Spectra were referenced to external adamantane.

2.8 FT-IR analysis

IR spectra of fully hydrated H-CH and D-CH samples were collected on a Perkin Elmer Spectrum 100 FT-IR spectrometer (Perkin Elmer Instruments, Waltham, Massachusetts, USA) using an ATR accessory with a single bounce diamond crystal. Spectra were recorded between 4000 and 600 cm^{-1} at a resolution of 4 cm^{-1} and 32 scans were added. A single-beam spectrum of the clean crystal was used as a background. After converting the spectra into absorbance units, the baselines were corrected using a straight line between 4000 and 600 cm^{-1}. Duplicate spectra were recorded and averaged for further analysis. All spectra were deconvoluted with a Lorentzian line shape, a half-width of 15 cm^{-1} and a resolution enhancement factor of 1.5 using Bessel apodization.

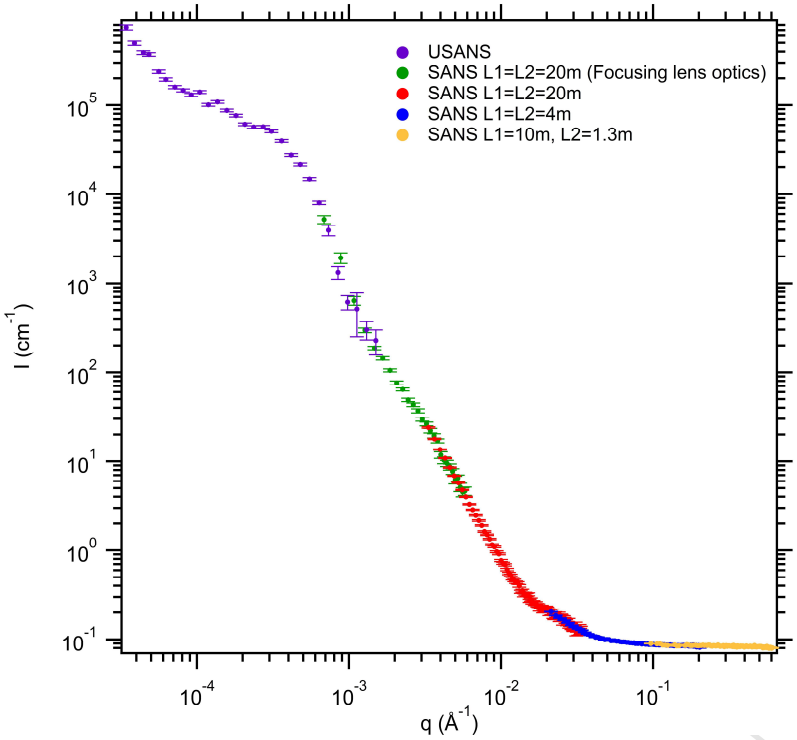

Figure 1. Merging of the experimental data for D-CH soaked in D_2O. The data corresponding to the four different SANS configurations and the USANS experiment are shown with different colours.

Table 1. Neutron and X-ray scattering length densities for protiated and deuterated bacterial cellulose. The following physical densities were used: ρ(crystalline cellulose) = 1.60 g/cm^3 [47], ρ(paracrystalline cellulose) = 1.51 g/cm^3 [48] and ρ(amorphous cellulose) = 1.48 g/cm^3 [49]. Bound H_2O and D_2O scattering length density values were calculated assuming a density increase of 25% with respect to the bulk solvent density, as reported in [47, 50].

	Neutron SLD (10^{10} cm^{-2})	X-ray SLD (10^{10} cm^{-2})
Cellulose (crystalline)	1.87	14.46
Cellulose (paracrystalline)	1.77	13.65

Cellulose (amorphous)	1.73	13.38
Cellulose (crystalline, D_2O exchanged)	3.66	---
Cellulose (amorphous, D_2O exchanged)	3.39	---
100% Deuterated cellulose (crystalline)	7.59	13.62
100% Deuterated cellulose (amorphous)	7.02	12.60
Hemicelluloses (*)	~ 1.62	~ 12.65
Bulk H_2O	-0.56	9.47
Bound H_2O	-0.70	11.84
D_2O	6.38	9.37
Bound D_2O	7.97	11.79

(*) The provided SLD value is based on the estimation previously conducted for tamarind XG and wheat AX [34]. However, this value should only be used as an approximation as it will differ depending on the molecular weight and degree of substitution of each particular hemicellulose.

3. Results and discussion

3.1 Construction and molecular analysis of cellulose hydrogels and its composites with PCW polysaccharides

After 48 h fermentation, the pure H-CH and D-CH, as well as the D-CH composite hydrogels form thick gelatinous pellicles at the liquid medium-air interface. The thickness of the synthesised hydrogels, as well as their wet weights and densities, are presented in Table 2. The differences in the estimated bulk densities may be indicative of D-CH being less dense than H-CH, suggesting that cellulose synthesis takes place at a slower rate when d-glucose is provided as the carbon source, as observed previously [3].

334 **Table 2.** Post ferementation characteristics of the pure and composite hydrogels.

	Hydrogel Thickness (mm)	Wet Weight (g)	Estimated Density (g/cm^3)	Polymer incorporation (%)
H-CH	1.11	2.46	1.64	---
D-CH	1.03	1.89	1.36	---
D-CH-AX	0.76	1.75	1.71	13
D-CH-XG	0.78	1.60	1.51	39
D-CH-MLG	1.05	2.94	2.07	32

335

336 Monosaccharide analysis of H-CH and D-CH reveals high purity, with >97% glucose
337 composition. When D-CH is produced in the presence of wheat endosperm AX, the level
338 of PCW polysaccharide incorporation is 13% AX. This is relatively low when compared to
339 the incorporation levels observed for H-CH-AX hydrogels, where the AX was dissolved by
340 vigorous overnight stirring in boiling water (ca. 50% AX) [14-16]. When barley
341 endosperm MLG is added to the fermentation medium, 32% MLG is incorporated into the
342 D-CH hydrogel, similar to previously reported values of 27-29% MLG incorporation for
343 H-CH-MLG [16, 53]. For the D-CH-XG hydrogel, incorporation of 39% XG is consistent
344 with previously reported values of ca. 27-38% XG for H-CH-XG samples [14-17].

345

346 **3.2 Microstructure characterisation**

347 The microstructures of the pure cellulose and composite hydrogels were visualised by
348 FESEM, and representative micrographs are presented in Figure 2. The soluble-extensive
349 fixing and critical-point drying sample preparation appeared to prevent microstructural
350 collapse of the highly hydrated samples during the drying process. FESEM revealed that

all the samples present the typical architecture of randomly oriented cellulose ribbons, which has been previously reported for cellulose hydrogels [3, 14-16, 22]. As the samples were only washed with water prior to the microscopy characterisation (to avoid any possible structural modifications caused by a more extensive washing with sodium hydroxide [54]), it was not possible to remove completely the bacteria cells, which are visible in the micrographs as cylindrical objects attached to the cellulose ribbons. The average ribbon cross-section values estimated from the FESEM micrographs are 27.7 ± 10.1 nm, 42.3 ± 14.4 nm, 33.7 ± 12.6 nm, 26.0 ± 10.4 nm and 34.0 ± 12.4 nm for H-CH, D-CH, D-CH-AX, D-CH-XG and D-CH-MLG, respectively. These values are similar to those observed for several bacterial cellulose samples [15, 24, 25, 35, 55, 56]. Given the large standard deviation values, the differences in the ribbon thickness are not significant.

As visualised in Figures 2D and 2E, it appears that XG and MLG act as cross-linking agents, promoting the association of ribbons. Thin strands of XG, acting as cross-bridges between cellulose ribbons, have previously been detected in H-CH-XG samples [14, 15]. In contrast with the marked molecular binding exhibited within D-CH-XG, D-CH-AX (Figure 2C) does not exhibit such features. In this latter composite hydrogel, small "nodules" (of ca. 78 ± 13 nm size) are visible (circled in Figure 2 and Figure S1). These are likely due to *in situ* precipitation by methanol during the solvent-rich sample preparation protocol, as previously reported [16]. Yet interestingly, in the D-CH-MLG micrographs (Figure 2E), a combination of a few nodular-like structures with an average size of ca. 57 ± 20 nm, consistent with earlier findings [16], as well as cross-linked cellulose ribbons are observed in the heterogeneous sample. The microarchitectural obervations made for D-CH-MLG in this study suggest that deuteration may promote non-covalent cross bridges to form between cellulose ribbons by MLG in the D-CH hydrogel.

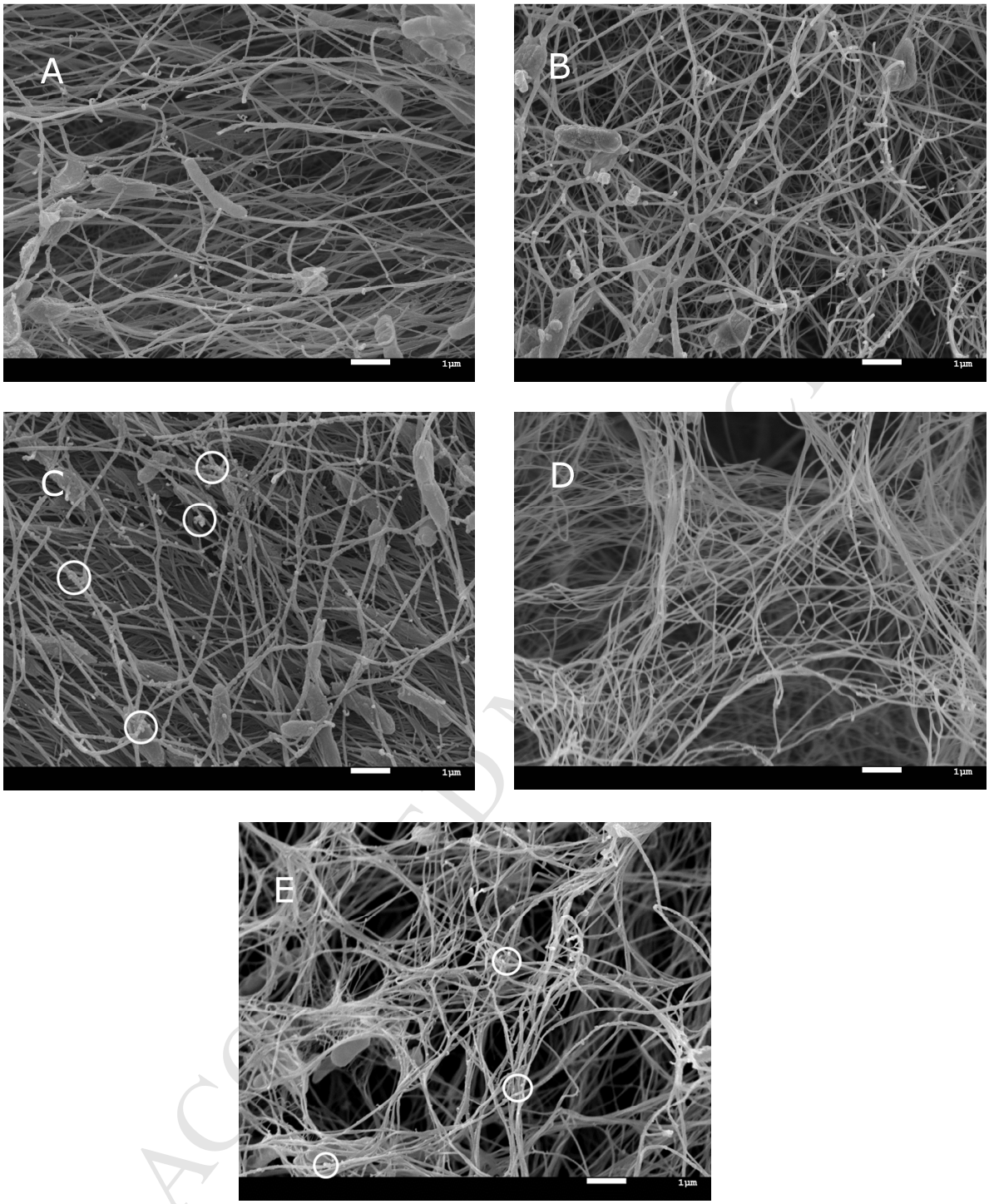

Figure 2. FESEM micrographs of freeze-subtituted H-CH (A), D-CH (B), D-CH-AX (C), D-CH-XG (D), and D-CH-MLG (E). Circles highlight some of the nodular structures detected in D-CH-AX and D-CH-MLG.

3.2 Molecular structure: ^{13}C CP/MAS NMR and FT-IR

The rigid components of the cellulose hydrogels were examined using solid-state ^{13}C CP/MAS NMR and the spectra obtained are displayed in Figure 3. The cellulose crystallinity index was estimated by integration of the signals at 85-92 ppm and at 80-85 ppm, corresponding to the internal crystalline and non-crystalline and/or crystal surface cellulose C4 sites respectively [57]. On the other hand, it was not possible to estimate the crystalline allomorph I_α/I_β ratio since, as previously noted [3], the peaks are complicated by the quadrupolar coupling between carbon and deuterium which splits the peak into multiplets.

In agreement with previous work [3, 30], the incorporation of deuterium into the cellulose molecular structure does not appear to significantly affect crystallinity, as indicated by the similar values of ca. 87 and 84% for H-CH and D-CH, respectively. With regards to the effect of the different PCW polysaccharides, while the incorporation of AX into the D-CH structure does not seem to induce any significant change in the crystallinity (X_C = 81%), a decrease is observed with the addition of MLG (X_C = 68%) and XG (X_C = 59%). The same trend of reduced crystallinity has been previously reported for composite H-CH hydrogels with XG (ca. 16% crystallinity reduction) [14] and MLG (ca. 7% crystallinity reduction) [16], although the effect seems to be stronger for the D-CH composite hydrogels.

The presence of XG in the rigid phase of D-CH-XG was confirmed by the detection of peaks located at 100 ppm and at 82 ppm, due to the C1 and C4 of xylose [14]. Calculating the ratio of the C1 xylose peak to the C1 cellulose peak, shows that the composite has ca. 18% XG bound to the cellulose (i.e. 46% of the XG is bound to cellulose), in agreement

411 with earlier studies [14]. In the case of D-CH-MLG, the spectrum shows a minor peak at
412 79-80 ppm that may be due to the C4 of MLG; however, if there were corresponding
413 signals for the expected C1 position at 102 ppm [16], they would be overlapped by the
414 cellulose C1 peak making it difficult to confirm. In this case, based on the ratio of the C4
415 MLG peak to the C4 cellulose peak, the amount of MLG bound to cellulose is only ca.
416 4%. It should be noted that all the samples contain more than 90% water and, thus, any
417 PCW polysaccharide which was not bound to cellulose would be mobile and would not be
418 observed in the ^{13}C CP/MAS experiment. Therefore, these results indicate that certain
419 fractions of XG (and possibly MLG) are bound to cellulose and potentially responsible for
420 the crystallinity decrease observed in the corresponding composite D-CH hydrogels.
421

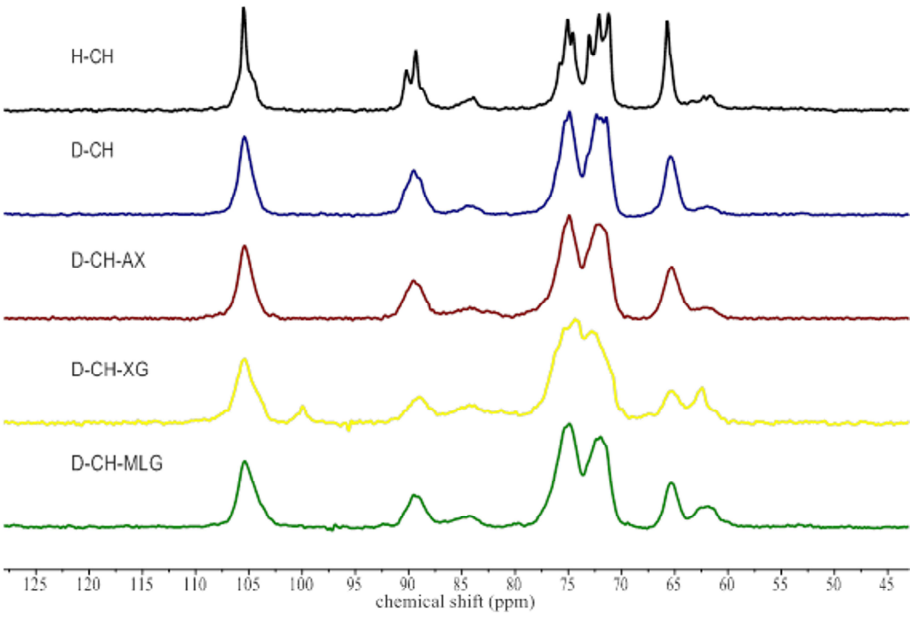

422

423 **Figure 3.** ^{13}C CP/MAS NMR of pure cellulose and composite hydrogels.

424

425 Figure 4 shows the region corresponding to the OH and CH stretching bands in the ATR-
426 FT-IR spectra of native H-CH and D-CH. As expected, both samples display characteristic
427 OH stretching bands in the region of 3500-3300 cm^{-1} [29, 30, 34]. The presence of OH

groups in D-CH is not surprising, since the OD groups originally present in the deuterated glucose are expected to be exchanged to OH groups after dissolving all the culture medium components in H_2O. On the other hand, the intensity of the bands appearing at 3000-2800 cm^{-1}, attributed to CH stretching [29, 30], is strongly reduced in the D-CH sample as compared with H-CH. The reduction in the area under this band has been previously used to estimate the degree of deuteration in D-CH, providing a value similar to that estimated, using an alternative approach, by determination of the sample neutron SLD through SANS contrast variation experiments [3]. In the present study, a reduction of ca. 81% in the area under the CH stretching bands is estimated by comparing the D-CH spectrum with that from H-CH. Considering that each glucose unit in the cellulose molecule contains seven CH groups, such a decrease corresponds to an average of ca 1.3 CH groups and 5.7 CD groups in the D-CH molecular structure; this suggests an average monomer structure between $C_6D_6H_4O_5$ and $C_6D_5H_5O_5$ for D-CH. A previous D-CH batch produced by using exactly the same method was reported to present a structure of $C_6D_5H_5O_5$, based on FT-IR and SANS contrast variation experiments [3]. Consequently, the molecular structure in the D-CH sample characterised in the present work is assumed to be closer to $C_6D_5H_5O_5$. FT-IR measurements were conducted on the hydrated material ex-H_2O; a monomer structure of $C_6D_7H_3O_5$, would be attained from a fully deuterated cellulose after the OD groups originally present in the deuterated glucose are exchanged to OH groups when dissolving the culture medium components in H_2O. In addition, the presence of other protiated components (such as peptone and yeast extract) in the culture medium and that are also involved in the *Komagataeibacter xylinus* glucose metabolism process inevitably further limits the degree of deuteration, as previously noted [3].

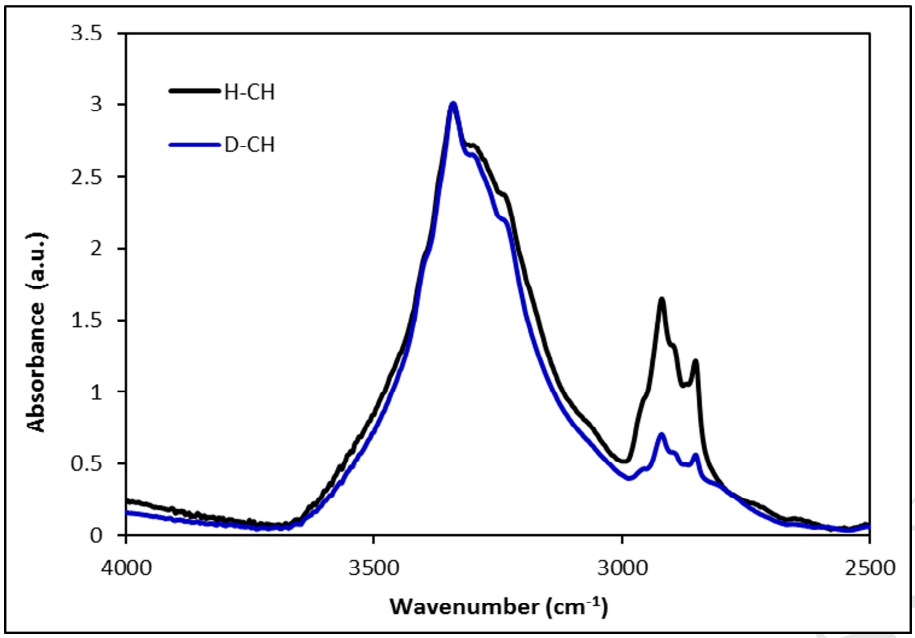

Figure 4. FT-IR spectra of H-CH and D-CH. Peaks are normalized to the OH stretch.

3.3 Micro- and nano-architecture: Combined USANS/SANS experiments

SANS and USANS experiments were carried out to characterise the structure of native H-CH and D-CH, as well as D-CH composites within the nano- and microscale size range. Samples were soaked in D_2O prior to the experiments, since the appearance of structural features associated with the cellulose ribbons has been previously shown to be optimised when using this solvent (as opposed to H_2O or H_2O/D_2O mixtures) as a result of H/D exchange undergone by the solvent held within the cellulose ribbons [2, 3]. Figure 5A shows the combined USANS/SANS data of the D_2O-soaked H-CH, D-CH and composite hydrogels. As observed, the combination of both techniques allowed a very broad q range to be covered of ca. 3×10^{-5} – 0.6 $Å^{-1}$. Several structural features, which can be more clearly identified in the corresponding Kratky plots (cf. Figure 5B), appear in the scattering patterns from all the samples. The shoulder features located within the region $0.01 < q / Å^{-1} < 0.10$ have been detected in the SANS patterns from protiated and deuterated cellulose hydrogels and arise from the existence of regions with distinct SLD values due to the sub-

structure of cellulose ribbons [2, 3, 15]. These shoulders are more intense in the case of D-CH and its composites, as compared with H-CH, due to a decreased contribution from interfacial scattering (i.e. decreased SLD contrast between the cellulose ribbons and the surrounding bulk D_2O) as a result of the partial deuteration within the cellulose molecular structure. Interestingly, two additional shoulder features, which have not been previously reported for cellulose hydrogels, appear within the region $3 \times 10^{-5} < q / Å^{-1} < 6 \times 10^{-3}$. It should be noted that, over the whole q range, the scattering intensity decreases with the deuteration level of the samples, with the highest intensity for H-CH and the lowest intensity for D-CH. This is again related to the decreased SLD contrast between the solvent and the partially deuterated cellulose in D-CH ($SLD_{D_2O} - SLD_{D-CH} = 6.38 - 4.75 = 1.63$ x 10^{10} cm^{-2}, assuming a structure of $C_6H_5D_5O_5$) compared to the SLD contrast with protiated cellulose in H-CH ($SLD_{D_2O} - SLD_{H-CH} = 6.38 - 1.84 = 4.54$ x 10^{10} cm^{-2}). In the case of the D-CH composites, the sample-solvent SLD contrast is expected to have intermediate values between those corresponding to H-CH and D-CH since they contain partially deuterated cellulose and protiated PCW polysaccharides.

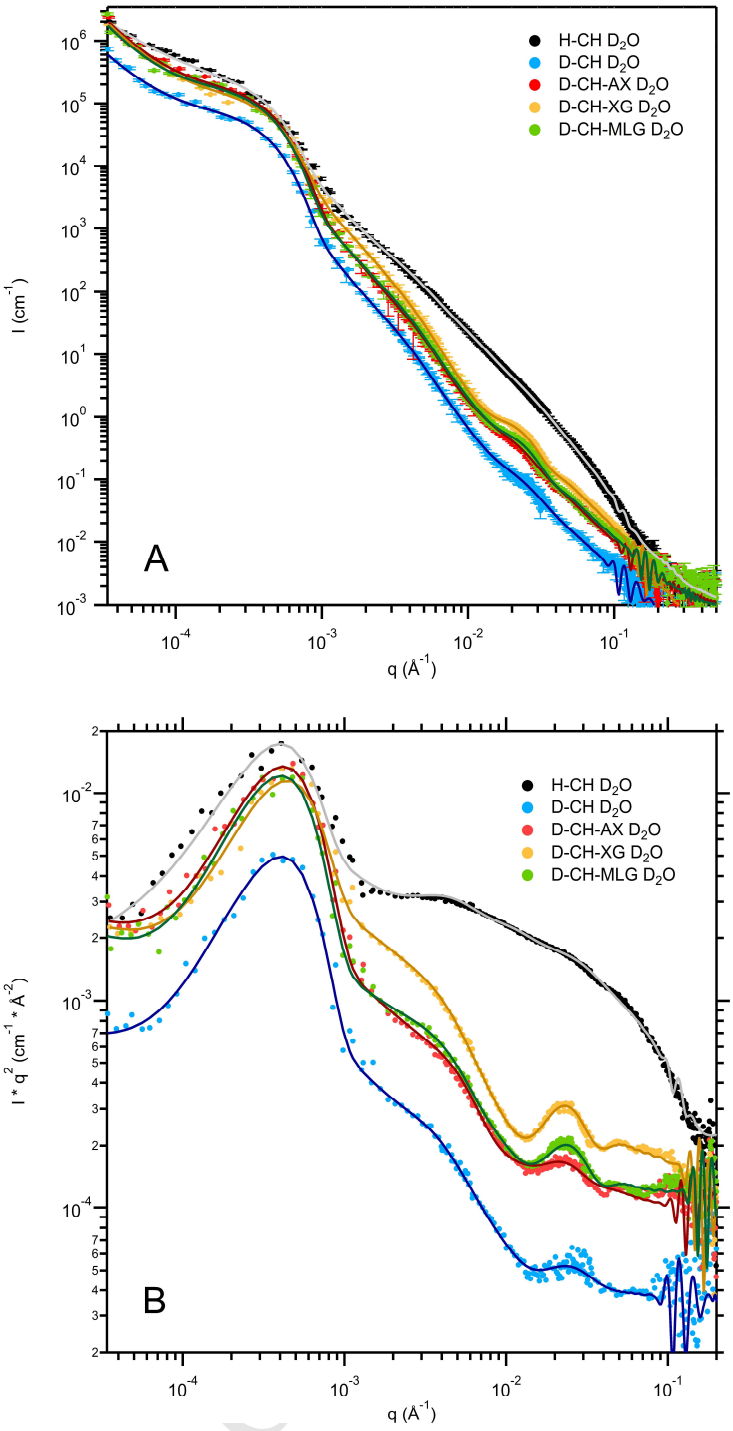

Figure 5. Combined USANS/SANS data for pure H-CH, D-CH and D-CH composites with PCW polysaccharides (soaked in D_2O) (A) and the corresponding Kratky plots (B). Solid lines correspond to the fitting of the experimental data using the sum model of a three-level Beaucage and a core-shell cylinder model.

Although a previous study reported on the USANS/SANS characterisation of bacterial cellulose covering a q range of 3 x 10^{-5} – 0.1 $Å^{-1}$, the data were interpreted merely by delimiting regions with different power-law exponents in the scattering curves [58]. It is possible to go far beyond this basic data interpretation and fully exploit the potential of combined USANS/SANS experiments by developing suitable models to fit the experimental data. However, the extremely complex structure of cellulose, which is hierarchically organised into different structural levels, has typically complicated the interpretation of small angle scattering data and only very recently has a model based upon a core-shell formalism been proposed to describe the SANS data from cellulose hydrogels [2, 3]. This core-shell formalism implicitly accounts for the sub-structure of cellulose microfibrils within ribbons and the role of moisture and, accordingly, it considers that cellulose ribbons are composed of two phases: (i) a core, containing impermeable crystallites surrounded by a network of paracrystalline cellulose and tightly bound water and (ii) a shell containing only paracrystalline cellulose and bound water. These two phases are expected to present different accessibility and H/D exchange when soaked in solvents, hence resulting in the formation of regions with distinct neutron SLD values. Based on this core-shell model, a function comprising the sum of a power-law term plus a core-shell cylinder with polydisperse radius was developed and applied to fit the SANS contrast variation data of protiated and deuterated cellulose hydrogels [2, 3]. The fitting function applied in the present study to fit the combined USANS/SANS data consisted of the sum of the core-shell cylinder with polydisperse radius term from the above described core-shell model (to describe the shoulder-like features detected at 0.01 < q / $Å^{-1}$ < 0.10) plus a three-level Beaucage model (to account for the additional structural features located within the 3 x 10^{-5} < q / $Å^{-1}$ < 6 x 10^{-3} range). As shown in Figures 5A and 5B, the sum model produces good fits across the wide intensity and q range considered

(over 9 orders of magnitude in intensity and 4 orders of magnitude in q). The values obtained for the refined parameters are summarised in Table 3.

The ribbon cross-section values estimated for H-CH (ca. 26.4 nm) and D-CH (ca. 29.2 nm) are very similar and consistent with the range of values estimated from the SEM characterisation. In agreement with previous results [3] and supporting the hypothesis of a slower synthesis rate, D-CH seems to present a less dense ribbon structure with a reduced cellulose volume fraction within the shell and greater H/D exchange in the cellulose contained within the core, as compared with H-CH. The overall ribbon cross-sections estimated for the composite D-CH hydrogels are ca. 29.9 nm, 28.8 nm and 27.1 nm for D-CH-AX, D-CH-XG and D-CH-MLG, respectively. Whereas the shell represents ca. 11% of the overall ribbon cross-section for D-CH-XG, it decreases to values of ca. 7% for D-CH-MLG and ca. 5% for D-CH-AX. This may be a result of strong cellulose-XG interactions being established. Close association between XG and the individual cellulose microfibrils is expected to disrupt the ribbon structure to a certain extent, promoting the accessibility of D_2O towards the inner region of the cellulose ribbons.

As expected, the strong hydrogen bonded network created between the cellulose microfibrils and bound water held within the core region limits the solvent accessibility and, as a result, the cellulose volume fraction within the ribbons' core is larger than the volume fraction within the shell. Interestingly, the incorporation of XG into D-CH leads to a decreased cellulose volume fraction within the core. The same behaviour was observed for H-CH incorporating XG, where it was attributed to the ability of this PCW polysaccharide to interact with the individual cellulose microfibrils contained within the ribbons' core [28].

542

543 The solvent exchange values indicate that ca. 20% of the water tightly bound to the
544 cellulose microfibrils within the core is not exchanged when the samples are soaked in
545 D_2O. Additionally, as indicated by the cellulose exchange values, the H/D exchange is
546 more limited within the core region due to the presence of non-accessible crystallites. It is
547 worth noting that the cellulose H/D exchange within the core is further restricted by the
548 incorporation of XG into the D-CH hydrogel. The addition of XG into H-CH has been
549 reported to show the same behaviour and is consistent with a reduction in the amount of
550 cellulose hydroxyl groups available for exchange due to the existence of strong cellulose-
551 XG interactions within the ribbons' core [28].

552

553 Consistent with the crystallinity reduction determined from NMR characterisation, the sum
554 model fit parameters associated with the core-shell formalism (i.e. the second term in
555 equation (1)) suggest that XG is able to interact directly with the individual microfibrils
556 composing the cellulose ribbons and is located both within the core and the shell of the
557 ribbons; in contrast, AX and MLG domains are mostly limited to the surface (i.e. shell) of
558 the ribbons. This result is in agreement with what has been previously reported for H-CH
559 composite hydrogels with AX and XG [2, 15, 59]. It has been hypothesised that whereas
560 AX interacts with cellulose once the crystallisation and aggregation of cellulose
561 microfibrils has been completed, XG can establish interactions with cellulose
562 simultaneously with the crystallisation/aggregation processes, hence promoting the
563 formation of fewer crystalline cellulose microfibrils richer in the I_β allomorph [15]. On the
564 other hand, the interaction mechanism of MLG with cellulose has not been clearly
565 established in the literature. Although MLG has been suggested to present a non-specific
566 surface adsorption interaction mechanism, analogous to that of AX based on the NMR

567 characterisation and mechanical properties of H-CH composites [16], a different study
568 showed that only 12-13% of MLG was removed from the wall of wheat and maize
569 coleoptiles by using a specific *endo*-(1→3)(1→4)-β-glucanase [60]. The results presented
570 here suggest that the ability of XG and MLG to disrupt interactions within and between
571 cellulose microfibrils during the crystallisation process may be linked to their cross-linking
572 role as is demonstrated by microscopy characterisation (cf. Figure 2). However, while XG
573 is able to establish strong interactions with the individual cellulose microfibrils, thus
574 remaining trapped within the ribbons' core, such strong interactions are limited in the case
575 of MLG which, in turn, interacts with cellulose mostly at the ribbons's surface level. Based
576 on our previous studies [2, 3], a more extensive characterisation of the D-CH composite
577 hydrogels is needed to fully understand the distinct interaction mechanisms of partially
578 deuterated cellulose and these PCW polysaccharides at the different relevant structural
579 levels. Future work will consist of SANS contrast variation experiments (which provide
580 information on the ribbon structural level), with SAXS and XRD characterisation (which
581 highlight the structural organisation of the individual cellulose microfibrils).
582
583 To the best of our knowledge, the shoulder-like features appearing in the lower q region
584 from the combined USANS/SANS data are reported here for the first time. To account for
585 these features, a term corresponding to a unified equation (i.e. Beaucage model) with three
586 structural levels was incorporated into the applied fitting function, as described in section
587 2.6. The Beaucage model has been previously utilised to fit the SANS data from
588 switchgrass lignocellulose, enabling the identification of morphological changes induced
589 by a diluted acid treatment [61]. As observed in Figures 5A and 5B, the structural features
590 within the $3 \times 10^{-5} < q / Å^{-1} < 6 \times 10^{-3}$ range are well described by using this mathematical
591 function.

The characteristic dimensions of the structural features detected in the USANS/SANS data can be estimated from the R_g values obtained. The cellulose network in the hydrogels is composed of ribbons, which may be considered as long core-shell cylindrical objects with cross-sections within the range of 20-40 nm [3]. At the same time, these ribbons are composed of cellulose microfibrils, which can also be simplified as core-shell cylindrical objects with an overall diameter of ca. 3.0-3.5 nm [3]. Considering this and taking into account the approximate q values at which the two features are located (ca. 3×10^{-4} Å^{-1} and 6×10^{-3} Å^{-1}), we propose that these shoulders arise from the structure of cellulose microfibrils and ribbons in the longitudinal axis direction, i.e. $R_{g,3}$ from the longitudinal arrangement of cellulose microfibrils and $R_{g,2}$ from structural features in the ribbon longitudinal direction. Assuming a cylindrical morphology for both the microfibrils and the ribbons, the corresponding lengths can be calculated by applying the following equation for R_g based on a cylindrical rod with length L and radius R:

$$R_{g,i}{}^2 = \frac{R_i{}^2}{2} + \frac{L_i{}^2}{12} \qquad (2)$$

where R_2 is assumed to be equal to the cross-section values estimated from the sum model fitting (cf. Table 3) and R_3 to the approximate cross-section reported for the impermeable crystalline core of cellulose microfibrils (i.e. 1.6 nm [3]). The calculated values for the characteristic lengths corresponding to $R_{g,2}$ and $R_{g,3}$ (L_2 and L_3, respectively) are: L_2=1468 ± 7 nm and L_3=142 ± 1 nm for H-CH, L_2=1470 ± 13 nm and L_3=180 ± 6 nm for D-CH, L_2=1422 ± 9 nm and L_3=150 ± 6 nm for D-CH-AX, L_2=1367 ± 6 nm and L_3=166 ± 6 nm for D-CH-XG and L_2=1474 ± 6 nm and L_3=166 ± 5 nm for D-CH-MLG.

The smallest characteristic length (L_3), which ranges between ca. 140-180 nm, may be associated with the length of the cellulose crystalline domains. To date, information regarding the morphology of bacterial cellulose crystallites has been inferred from subjecting the native material to hydrolysis treatments. Based on microscopy characterisation, cellulose nanocrystals extracted by acid hydrolysis of bacterial cellulose have been reported to have lengths within the range of 100 nm to several μm [32-37]. The large variability in the length values is related to the heterogeneity in the acid hydrolysis procedures applied to extract these nanocrystals. It is known that several factors such as acid concentration, temperature and hydrolysis time have a strong effect on the extent to which the amorphous and paracrystalline domains are digested [34, 36] and consequently hydrolysis treatments with different characteristic parameters are expected to yield nanocrystals with distinct morphologies. It should be considered that the longer rod-like structures extracted by acid hydrolysis of bacterial cellulose have been shown to correspond to aggregates of 3-6 microfibrils rather than to individual crystallites [35]. Hence, the cellulose crystalline domain lengths may be smaller than some of the values previously estimated from acid-digested materials, especially when milder hydrolysis conditions are applied. As deduced from the L_3 values, the cellulose crystallites in D-CH (ca. 180 nm) are larger than the crystallites in H-CH (ca. 142 nm). This suggests that the incorporation of deuterium atoms into the cellulose molecular structure has an effect on the synthesis process. As discussed above, it is probable that when d-glucose, instead of h-glucose, is provided as the carbon source, the bacteria synthesise cellulose at a slower rate. This has been previously hypothesised as the potential cause for the less dense ribbon structure detected in D-CH compared to H-CH [3]. Although no connection between the synthesis process and the morphology of the produced cellulose crystallites has been established in the literature, it is likely that, at a slower synthesis rate, the distance between

642 the defective regions (i.e. cellulose amorphous domains) increases; to demonstrate this,
643 identical acid hydrolysis treatments could be applied to H-CH and D-CH samples to
644 confirm whether the length of the extracted crystallites is significantly different. Moreover,
645 the incorporation of PCW polysaccharides into D-CH appears to induce the formation of
646 slightly shorter crystallites which may arise from the establishment of interactions between
647 the amorphous cellulose domains and a fraction of the PCW polysaccharides. However,
648 these results should be interpreted with caution, as the same crystallite radius was used to
649 estimate the crystallite length for all the samples. This assumption seems valid in the case
650 of AX which, according to previous XRD characterisation, does not induce any significant
651 modification in the cellulose crystallite cross-section [15]. In contrast, smaller crystallites
652 have been observed for H-CH composite hydrogels with XG [15] and, consequently, the
653 actual D-CH-XG crystallite length may be larger than the estimated value. Since the
654 microfibril crystalline core radius can be determined by fitting the complementary SAXS
655 data from cellulose hydrogels [2, 3], future work using SAXS characterisation to
656 accurately determine the crystallite lengths for the pure and composite cellulose hydrogels
657 would be beneficial.
658
659 At the next structural level, bacterial cellulose ribbons have been reported to be
660 periodically twisted along their longitudinal axis [55, 56, 62-64]. The mechanism leading
661 to the development of twists has not yet been established. An initial hypothesis claimed
662 that the twists could be created from the rotation of bacterial cellulose along its
663 longitudinal axis [63]. However, it was demonstrated that the origin of these twists is more
664 likely related to the intrinsic chirality of cellulose molecules [65, 66]. Based upon TEM
665 images, the ribbon twisting periodicity has been estimated as ca. 1 μm [64, 67]. Moreover,
666 mild acid digestion of bacterial cellulose has been reported to produce structures consisting

667 of microfibril aggregates with an average length of ca. 1.2 μm [35]. If the twisting regions
668 are considered as less structurally stable domains, then the mild acid hydrolysis applied in
669 the cited work could proceed by disrupting the ribbon structure preferentially through the
670 twisting domains. The values reported in the literature for the ribbon twisting periodicity
671 are similar to the 1.4-1.5 μm characteristic lengths (L_2) estimated for the pure and
672 composite hydrogels. Nevertheless, it is also the case that different structural entities, such
673 as bacteria cells remaining in the samples or water-filled pores in the hydrogel network
674 structure could, in principle, also be responsible for the appearance of the shoulder-like
675 feature detected in the scattering patterns. The dimensions of the remaining bacteria cells
676 are ca. 447 ± 133 nm x 1735 ± 624 nm, as measured from SEM images. If the cell is
677 considered to present a cylindrical shape, then the associated R_g value would be ca. 525
678 nm. This value does not agree well with the R_g values provided by the unified fits and it is
679 unlikely that the presence of bacteria cells is the source of the scattering feature; however,
680 collecting the scattering patterns from hydrogel samples washed with NaOH to remove any
681 bacteria cell debris would be desirable to fully discard this as a possibility. With regards to
682 the water-filled pores in the hydrogel network structure, direct measurements from the
683 SEM images (albeit with the caveat of the possibility of sample drying artefacts) indicate
684 that the average pore size is ca. 500 ± 300 nm in the case of H-CH, D-CH and D-CH-AX,
685 whereas it reduces to ca. 300 ± 200 nm for the D-CH-XG and D-CH-MLG composites.
686 Thus, it also seems implausible that the shoulder features arise from the contrast between
687 the water-filled pores and the ribbons, since the pore size does not match the q range at
688 which the shoulders are located and it is also not modified by the incorporation of PCW
689 polysaccharides. If the hypothesis of the shoulder feature arising from the ribbon twisting
690 periodicity is correct, the results would indicate that neither the partial deuteration of the
691 cellulose molecular structure nor the incorporation of PCW polysaccharides would have a

692 strong effect on the distance between two consecutive twists which is shown here to
693 remain approximately constant at ca. 1.4-1.5 μm for all hydrogel samples.
694
695 These results demonstrate the great potential of combining SANS and USANS
696 experiments to characterise the multi-scale architecture of cellulose hydrogels, covering
697 the size range relevant to the cellulose structural organisation in both the cross-sectional
698 and longitudinal directions. In particular, the extended q range provided by USANS has
699 enabled the identification of structural features on the micron size range in cellulose
700 hydrogels. Based on prior knowledge of the system, it has been hypothesised that the
701 observed shoulder-like features arise from the arrangement of crystalline/amorphous
702 cellulose domains along the microfibril and from periodic ribbon twisting. If that is the
703 case, USANS experiments would be extremely valuable to answer relevant questions that
704 still remain open in this research area such as whether different bacterial strains, with
705 distinct synthesis rates, are able to synthesise cellulose crystallites with varying
706 morphologies or how the cellulose network structure is progressively broken down when
707 subjecting native hydrogels to acid hydrolysis treatments.
708
709 **Table 3.** Parameters obtained from fits of the sum model (three-level Beaucage plus core-
710 shell cylinder with polydisperse radius) for native H-CH, D-CH and D-CH composites
711 with PCW polysaccharides (soaked in D_2O). Standard deviations on the last digit are
712 shown in parentheses.

	H-CH	D-CH	D-CH-AX	D-CH-XG	D-CH-MLG
Scale factor	0.0183(1)	0.0209(3)	0.050(1)	0.0450(2)	0.050(4)
Core radius (nm)	9.44(9)	13.68(3)	14.2(2)	12.75(5)	12.58(8)
Core length (nm) (*)	500.0	500.0	500.0	500.0	500.0

Polydispersity	0.376(3)	0.288(8)	0.254(4)	0.234(1)	0.229(2)
Radial shell thickness (nm)	3.78(3)	0.91(1)	0.76(1)	1.65(2)	0.98(6)
Cellulose volume fraction (Core)	0.218(2)	0.212(2)	0.168(4)	0.119(2)	0.232(4)
Cellulose volume fraction (Shell)	0.038(1)	0.001(1)	0.001(3)	0.093(1)	0.001(5)
Cellulose exchange (core)	0.48(1)	0.60(3)	0.60(1)	0.35(1)	0.63(1)
Cellulose exchange (shell)	1.0(6)	0.6(3)	1.0(3)	0.37(2)	1.0(1)
Solvent exchange (core)	0.825(1)	0.821(1)	0.824(1)	0.803(2)	0.814(1)
Solvent exchange (shell) (*)	1.00	1.00	1.00	1.00	1.00
SLD cellulose (10^{10} cm^{-2}) (*)	1.85	4.76	4.75	4.67	4.71
SLD fully exchanged cellulose (10^{10} cm^{-2}) (*)	3.63	6.43	6.41	6.31	6.35
SLD bulk solvent (10^{10} cm^{-2}) (*)	6.38	6.38	6.38	6.38	6.38
SLD bound solvent (10^{10} cm^{-2}) (*)	7.97	7.97	7.97	7.97	7.97
SLD bound H_2O (10^{10} cm^{-2}) (*)	-0.70	-0.70	-0.70	-0.70	-0.70
B_1 ($cm^{-1}\cdot sr^{-1}$)	0.05(2)	$7(2)\cdot 10^{-5}$	$7(2)\cdot 10^{-5}$	$6(3)\cdot 10^{-5}$	$2(1)\cdot 10^{-5}$
PL_1	1.69(3)	2.211(3)	2.34(6)	2.34(6)	2.44(7)

G_2 ($cm^{-1}\cdot sr^{-1}$)	$2.48(4)\cdot 10^5$	$7.8(1)\cdot 10^5$	$2.01(4)\cdot 10^5$	$1.55(4)\cdot 10^5$	$1.95(4)\cdot 10^5$
$R_{g,2}$ (nm)	424(4)	425(4)	411(3)	395(4)	426(3)
B_2 ($cm^{-1}\cdot sr^{-1}$)	$0.2(1)\cdot 10^{-6}$	$2(1)\cdot 10^{-6}$	$12(7)\cdot 10^{-6}$	$50(10)\cdot 10^{-6}$	$20(10)\cdot 10^{-6}$
PL_2	2.75(7)	2.8(2)	2.70(9)	2.59(9)	2.6(1)
G_3 ($cm^{-1}\cdot sr^{-1}$)	$0.36(3)\cdot 10^3$	$0.4(1)\cdot 10^3$	$0.5(1)\cdot 10^3$	$1.3(4)\cdot 10^3$	$0.9(2)\cdot 10^3$
$R_{g,3}$ (nm)	41(1)	52(3)	43(2)	48(3)	48(2)
B_3 ($cm^{-1}\cdot sr^{-1}$)	$0.43(1)\cdot 10^{-6}$	$0.031(2)\cdot 10^{-6}$	$9.4(1)\cdot 10^{-6}$	$0.018(6)\cdot 10^{-6}$	$0.18(5)\cdot 10^{-6}$
PL_3	2.865(6)	3.63(8)	2.62(3)	4.00(7)	3.50(6)

Parameters displayed with $^{(*)}$ were fixed during the fitting process.

4. Conclusions

Partially deuterated cellulose hydrogels (D-CH), and resultant composites with three major PCW polysaccharides (AX, XG and MLG), were synthesised by using d-glucose as the carbon source in the fermentation medium of *Komagataeibacter xylinus*. PCW polysaccharide incorporation into the hydrogels has been confirmed by monosaccharide analyses, while their effect on the multi-scale architecture of D-H has been investigated by combined USANS/SANS experiments and complementary microscopy and spectroscopy techniques. The combination of SANS with USANS enabled the coverage of four orders of magnitude in q and revealed unique structural features characteristic of the very broad size range explored that is highly relevant to the multi-scale architecture of cellulose hydrogels.

The structural features located within the range $0.01 < q / Å^{-1} < 0.10$ are well-described by the core-shell cylinder model included in the sum fitting function. This core-shell model accounts for the sub-structure of cellulose microfibrils within ribbons and for the role of moisture. The fitting results suggest that only XG is able to establish strong interactions

with the individual cellulose microfibrils, thus affecting the properties of the cellulose ribbons' core; in contrast, cellulose-AX and cellulose-MLG interactions are mostly limited to the ribbons' surface. On the other hand, the ^{13}C-NMR results indicate that the presence of XG or MLG at the time of cellulose synthesis is able to perturb cellulose at the microfibril structural level, leading to reduced crystallinity values. This effect seems to be linked to their ribbon cross-linking role as revealed by SEM characterisation.

Furthermore, an additional term consisting of a unified three-level function was included into the fitting function to account for the two shoulder-like features appearing within the range $3 \times 10^{-5} < q / Å^{-1} < 6 \times 10^{-3}$, which are reported for the first time for cellulosic materials. Considering a cylindrical morphology, features characteristic of length scales of 140-180 nm and ca. 1.4-1.5 μm along the microfibrils and ribbon longitudinal axis, respectively have been identified. Based on the corresponding size ranges and prior knowledge of the cellulose structure, the first feature is proposed to arise from the length of cellulose crystallites, whereas the second feature is attributed to the ribbon twisting periodicity. In addition, the fitting results indicate that the crystallite length increases due to the potentially slower D-CH synthesis rate (*cf* H-CH); this hypothesis is in agreement with the larger and less dense ribbon structure observed for D-CH. The incorporation of PCW polysaccharides into D-CH appears to induce the formation of slightly shorter crystallites, which may originate from the establishment of interactions between these polysaccharides and the amorphous cellulose domains. In the presence of PCW polysaccharides, no effect is found on the ribbon twisting.

This study has demonstrated the potential of combined USANS/SANS experiments to elucidate the multi-scale structure of cellulose hydrogels. In particular, USANS is

754 presented as a promising technique which may be extremely useful to investigate the
755 structural arrangement of cellulose in the longitudinal direction. This is expected to
756 provide valuable insights into understanding the cellulose biosynthesis process,
757 fundamental to plant biology, and to determine the mechanism of cellulose digestion when
758 subjected to hydrolysis treatments which is of relevance to diverse areas such as the
759 optimisation of biofuels' synthesis processes and the development of bio-based and
760 biodegradable materials.

761

762 **Acknowledgements**

763 Dr. Dongjie Wang is acknowledged for the SEM characterisation of cellulose hydrogel
764 samples. MMS would like to acknowledge a postdoctoral fellowship jointly funded by
765 ANSTO and the ARC Centre of Excellence in Plant Cell Walls.

766

767 **References**

768 [1] M. Iguchi, S. Yamanaka, and A. Budhiono, Bacterial cellulose - a masterpiece of
769 nature's arts, Journal of Materials Science 35 (2000) 261-270.
770 [2] M. Martinez-Sanz, M.J. Gidley, and E.P. Gilbert, Hierarchical architecture of
771 bacterial cellulose and composite plant cell wall polysaccharide hydrogels using
772 small angle neutron scattering, Soft Matter 12 (2016) 1534-1549.
773 [3] M. Martínez-Sanz, D. Mikkelsen, B. Flanagan, M.J. Gidley, and E.P. Gilbert, Multi-
774 scale model for the hierarchical architecture of native cellulose hydrogels,
775 Carbohydrate Polymers in press (2016)
776 [4] G. Helenius, H. Bäckdahl, A. Bodin, U. Nannmark, P. Gatenholm, and B. Risberg,
777 In vivo biocompatibility of bacterial cellulose, Journal of Biomedical Materials
778 Research Part A 76A (2006) 431-438.
779 [5] L. Nimeskern, H. Martínez Ávila, J. Sundberg, P. Gatenholm, R. Müller, and K.S.
780 Stok, Mechanical evaluation of bacterial nanocellulose as an implant material
781 for ear cartilage replacement, Journal of the Mechanical Behavior of Biomedical
782 Materials 22 (2013) 12-21.
783 [6] S. Zang, R. Zhang, H. Chen, Y. Lu, J. Zhou, X. Chang, G. Qiu, Z. Wu, and G. Yang,
784 Investigation on artificial blood vessels prepared from bacterial cellulose,
785 Materials Science and Engineering: C 46 (2015) 111-117.
786 [7] Z. Shi, Y. Zhang, G.O. Phillips, and G. Yang, Utilization of bacterial cellulose in
787 food, Food Hydrocolloids 35 (2014) 539-545.

[8] E. Fortunati, I. Armentano, Q. Zhou, A. Iannoni, E. Saino, L. Visai, L.A. Berglund, and J.M. Kenny, Multifunctional bionanocomposite films of poly(lactic acid), cellulose nanocrystals and silver nanoparticles, Carbohydrate Polymers 87 (2012) 1596-1605.

[9] M. Martínez-Sanz, A. Lopez-Rubio, and J.M. Lagaron, Optimization of the dispersion of unmodified bacterial cellulose nanowhiskers into polylactide via melt compounding to significantly enhance barrier and mechanical properties, Biomacromolecules 13 (2012) 3887-3899.

[10] M. Nogi and H. Yano, Transparent nanocomposites based on cellulose produced by bacteria offer potential innovation in the electronics device industry, Advanced Materials 20 (2008) 1849-1852.

[11] E. Ten, J. Turtle, D. Bahr, L. Jiang, and M. Wolcott, Thermal and mechanical properties of poly(3-hydroxybutyrate-co-3-hydroxyvalerate)/cellulose nanowhiskers composites, Polymer 51 (2010) 2652-2660.

[12] E. Chanliaud and M.J. Gidley, In vitro synthesis and properties of pectin/Acetobacter xylinus cellulose composites, Plant Journal 20 (1999) 25-35.

[13] D. Lin, P. Lopez-Sanchez, and M.J. Gidley, Interactions of pectins with cellulose during its synthesis in the absence of calcium, Food Hydrocolloids 52 (2016) 57-68.

[14] P. Lopez-Sanchez, J. Cersosimo, D. Wang, B. Flanagan, J.R. Stokes, and M.J. Gidley, Poroelastic Mechanical Effects of Hemicelluloses on Cellulosic Hydrogels under Compression, PLoS ONE 10 (2015) e0122132.

[15] M. Martínez-Sanz, P. Lopez-Sanchez, M.J. Gidley, and E.P. Gilbert, Evidence for differential interaction mechanism of plant cell wall matrix polysaccharides in hierarchically-structured bacterial cellulose, Cellulose 22 (2015) 1541-1563.

[16] D. Mikkelsen, B.M. Flanagan, S.M. Wilson, A. Bacic, and M.J. Gidley, Interactions of Arabinoxylan and (1,3)(1,4)-β-Glucan with Cellulose Networks, Biomacromolecules 16 (2015) 1232-1239.

[17] S.E.C. Whitney, J.E. Brigham, A.H. Darke, J.S.G. Reid, and M.J. Gidley, In vitro assembly of cellulose/xyloglucan networks: ultrastructural and molecular aspects, The Plant Journal 8 (1995) 491-504.

[18] S.E.C. Whitney, J.E. Brigham, A.H. Darke, J.S.G. Reid, and M.J. Gidley, Structural aspects of the interaction of mannan-based polysaccharides with bacterial cellulose, Carbohydrate Research 307 (1998) 299-309.

[19] R. Yokoyama and K. Nishitani, Genomic Basis for Cell-Wall Diversity in Plants. A Comparative Approach to Gene Families in Rice and Arabidopsis, Plant and Cell Physiology 45 (2004) 1111-1121.

[20] Y.B. Park and D.J. Cosgrove, Changes in Cell Wall Biomechanical Properties in the Xyloglucan-Deficient xxt1/xxt2 Mutant of Arabidopsis, Plant Physiology 158 (2012) 465-475.

[21] J. Gu and J.M. Catchmark, The impact of cellulose structure on binding interactions with hemicellulose and pectin, Cellulose 20 (2013) 1613-1627.

[22] P. Lopez-Sanchez, M. Rincon, D. Wang, S. Brulhart, J.R. Stokes, and M.J. Gidley, Micromechanics and poroelasticity of hydrated cellulose networks, Biomacromolecules 15 (2014) 2274-2284.

[23] Y.B. Park, C.M. Lee, K. Kafle, S. Park, D.J. Cosgrove, and S.H. Kim, Effects of plant cell wall matrix polysaccharides on bacterial cellulose structure studied with vibrational sum frequency generation spectroscopy and x-ray diffraction, Biomacromolecules 15 (2014) 2718-2724.

[24] C. Tokoh, K. Takabe, M. Fujita, and H. Saiki, Cellulose synthesized by Acetobacter xylinum in the presence of acetyl glucomannan, Cellulose 5 (1998) 249-261.
[25] C. Tokoh, K.J. Takabe, and M. Fujita, Cellulose synthesized by Acetobacter xylinum in the presence of plant cell wall polysaccharides, Cellulose 9 (2002) 65-74.
[26] K.I. Uhlin, R.H. Atalla, and N.S. Thompson, Influence of hemicelluloses on the aggregation patterns of bacterial cellulose, Cellulose 2 (1995) 129-144.
[27] S.E.C. Whitney, E. Wilson, J. Webster, A. Bacic, J.S.G. Reid, and M.J. Gidley, Effects of structural variation in xyloglucan polymers on interactions with bacterial cellulose, American Journal of Botany 93 (2006) 1402-1414.
[28] M. Martínez-Sanz, M.J. Gidley, and E.P. Gilbert, Application of X-ray and neutron small angle scattering techniques to study the hierarchical structure of plant cell walls: a review, Carbohydrate Polymers 125 (2015) 120-134.
[29] G. Bali, M.B. Foston, H.M. O'Neill, B.R. Evans, J. He, and A.J. Ragauskas, The effect of deuteration on the structure of bacterial cellulose, Carbohydrate Research 374 (2013) 82-88.
[30] J. He, S.V. Pingali, S.P.S. Chundawat, A. Pack, A.D. Jones, P. Langan, B.H. Davison, V. Urban, B. Evans, and H. O'Neill, Controlled incorporation of deuterium into bacterial cellulose, Cellulose 21 (2014) 927-936.
[31] R.A. Russell, C.J. Garvey, T.A. Darwish, L.J.R. Foster, and P.J. Holden. Chapter Five - Biopolymer Deuteration for Neutron Scattering and Other Isotope-Sensitive Techniques. In: Zvi K, editor. Methods in Enzymology, vol. Volume 565: Academic Press, 2015. pp. 97-121.
[32] J. Araki and S. Kuga, Effect of Trace Electrolyte on Liquid Crystal Type of Cellulose Microcrystals, Langmuir 17 (2001) 4493-4496.
[33] A. Hirai, O. Inui, F. Horii, and M. Tsuji, Phase Separation Behavior in Aqueous Suspensions of Bacterial Cellulose Nanocrystals Prepared by Sulfuric Acid Treatment, Langmuir 25 (2009) 497-502.
[34] M. Martínez-Sanz, A. Lopez-Rubio, and J. Lagaron, Optimization of the nanofabrication by acid hydrolysis of bacterial cellulose nanowhiskers, Carbohydrate Polymers 85 (2011) 228-236.
[35] R.T. Olsson, R. Kraemer, A. Lopez-Rubio, S. Torres-Giner, M.J. Ocio, and J.M. Lagaron, Extraction of microfibrils from bacterial cellulose networks for electrospinning of anisotropic biohybrid fiber yarns, Macromolecules 43 (2010) 4201-4209.
[36] M. Roman and W.T. Winter, Effect of Sulfate Groups from Sulfuric Acid Hydrolysis on the Thermal Degradation Behavior of Bacterial Cellulose, Biomacromolecules 5 (2004) 1671-1677.
[37] I.A. Sacui, R.C. Nieuwendaal, D.J. Burnett, S.J. Stranick, M. Jorfi, C. Weder, E.J. Foster, R.T. Olsson, and J.W. Gilman, Comparison of the Properties of Cellulose Nanocrystals and Cellulose Nanofibrils Isolated from Bacteria, Tunicate, and Wood Processed Using Acid, Enzymatic, Mechanical, and Oxidative Methods, ACS Applied Materials & Interfaces 6 (2014) 6127-6138.
[38] S. Hestrin and M. Schramm, Synthesis of cellulose by Acetobacter xylinum. 2. Preparation of freeze-dried cells capable of polymerizing glucose to cellulose, Biochemical Journal 58 (1954) 345-352.

[39] D. Mikkelsen and M.J. Gidley, Formation of cellulose-based composites with hemicelluloses and pectins using Gluconacetobacter fermentation, Methods in molecular biology (Clifton, N.J.) 715 (2011) 197-208.
[40] F.A. Pettolino, C. Walsh, G.B. Fincher, and A. Bacic, Determining the polysaccharide composition of plant cell walls, Nat. Protocols 7 (2012) 1590-1607.
[41] M.D. Abràmoff, P.J. Magalhães, and S.J. Ram, Image processing with imageJ, Biophotonics International 11 (2004) 36-41.
[42] E.P. Gilbert, J.C. Schulz, and T.J. Noakes, 'Quokka'-the small-angle neutron scattering instrument at OPAL, Physica B: Condensed Matter 385-386 (2006) 1180-1182.
[43] S. Kline, Reduction and analysis of SANS and USANS data using IGOR Pro, Journal of Applied Crystallography 39 (2006) 895-900.
[44] C. Rehm, A. Brule, A.K. Freund, and S.J. Kennedy, Kookaburra: the ultra-small-angle neutron scattering instrument at OPAL, Journal of Applied Crystallography 46 (2013) 1699-1704.
[45] G. Beaucage, Approximations Leading to a Unified Exponential/Power-Law Approach to Small-Angle Scattering, Journal of Applied Crystallography 28 (1995) 717-728.
[46] G. Beaucage, Small-Angle Scattering from Polymeric Mass Fractals of Arbitrary Mass-Fractal Dimension, Journal of Applied Crystallography 29 (1996) 134-146.
[47] A.P. Heiner and O. Teleman, Interface between Monoclinic Crystalline Cellulose and Water: Breakdown of the Odd/Even Duplicity, Langmuir 13 (1997) 511-518.
[48] M. Ioelovich, A. Leykin, and O. Figovsky, Study of cellulose paracrystallinity, BioResources 5 (2010) 1393-1407.
[49] W. Chen, G.C. Lickfield, and C.Q. Yang, Molecular modeling of cellulose in amorphous state. Part I: model building and plastic deformation study, Polymer 45 (2004) 1063-1071.
[50] J.F. Matthews, C.E. Skopec, P.E. Mason, P. Zuccato, R.W. Torget, J. Sugiyama, M.E. Himmel, and J.W. Brady, Computer simulation studies of microcrystalline cellulose Iβ, Carbohydrate Research 341 (2006) 138-152.
[51] A. Krystynowicz, W. Czaja, A. Wiktorowska-Jezierska, M. Gonçalves-Miśkiewicz, M. Turkiewicz, and S. Bielecki, Factors affecting the yield and properties of bacterial cellulose, Journal of Industrial Microbiology and Biotechnology 29 (2002) 189-195.
[52] K.A. Zahan, N. Pa'e, and I.I. Muhamad, Monitoring the Effect of pH on Bacterial Cellulose Production and Acetobacter xylinum 0416 Growth in a Rotary Discs Reactor, Arabian Journal for Science and Engineering 40 (2015) 1881-1885.
[53] D. Mikkelsen, M.J. Gidley, and B.A. Williams, In vitro fermentation of bacterial cellulose composites as model dietary fibers, Journal of Agricultural and Food Chemistry 59 (2011) 4025-4032.
[54] B.A. McKenna, D. Mikkelsen, J.B. Wehr, M.J. Gidley, and N.W. Menzies, Mechanical and structural properties of native and alkali-treated bacterial cellulose produced by Gluconacetobacter xylinus strain ATCC 53524, Cellulose 16 (2009) 1047-1055.

[55] A.R. White and R.M. Brown, Enzymatic hydrolysis of cellulose: Visual characterization of the process, Proceedings of the National Academy of Sciences 78 (1981) 1047-1051.
[56] K. Zhang, Illustration of the development of bacterial cellulose bundles/ribbons by Gluconacetobacter xylinus via atomic force microscopy, Applied Microbiology and Biotechnology 97 (2013) 4353-4359.
[57] M. Foston, Advances in solid-state NMR of cellulose, Current Opinion in Biotechnology 27 (2014) 176-184.
[58] S. Koizumi, Z. Yue, Y. Tomita, T. Kondo, H. Iwase, D. Yamaguchi, and T. Hashimoto, Bacterium organizes hierarchical amorphous structure in microbial cellulose, European Physical Journal E 26 (2008) 137-142.
[59] P. Lopez-Sanchez, E. Schuster, D. Wang, M.J. Gidley, and A. Strom, Diffusion of macromolecules in self-assembled cellulose/hemicellulose hydrogels, Soft Matter 11 (2015) 4002-4010.
[60] S.N. Kiemle, X. Zhang, A.R. Esker, G. Toriz, P. Gatenholm, and D.J. Cosgrove, Role of (1,3)(1,4)-β-glucan in cell walls: Interaction with cellulose, Biomacromolecules 15 (2014) 1727-1736.
[61] S.V. Pingali, V.S. Urban, W.T. Heller, J. McGaughey, H. O'Neill, M. Foston, D.A. Myles, A. Ragauskas, and B.R. Evans, Breakdown of Cell Wall Nanostructure in Dilute Acid Pretreated Biomass, Biomacromolecules 11 (2010) 2329-2335.
[62] R.M. Brown Jr, The biosynthesis of cellulose, Journal of Macromolecular Science - Pure and Applied Chemistry 33 (1996) 1345-1373.
[63] A. Hirai, M. Tsuji, and F. Horii, Helical Sense of Ribbon Assemblies and Splayed Microfibrils of Bacterial Cellulose, Sen'i Gakkaishi 54 (1998) 506-510.
[64] M. Takai and S. Watanabe, Biosynthesis of Cellulose by Acetobacter Xylinum. II. Morphological Observations on the Formation of Cellulose Microfibrils by Acetobacter Xylinum, Polym J 7 (1975) 147-156.
[65] A.J. Bowling, Y. Amano, R. Lindstrom, and R.M. Brown, Rotation of Cellulose Ribbons During Degradation with Fungal Cellulase, Cellulose 8 (2001) 91-97.
[66] M. Khandelwal and A. Windle, Origin of chiral interactions in cellulose supra-molecular microfibrils, Carbohydrate Polymers 106 (2014) 128-131.
[67] A. Hirai, M. Tsuji, H. Yamamoto, and F. Horii, In Situ Crystallization of Bacterial Cellulose III. Influences of Different Polymeric Additives on the Formation of Microfibrils as Revealed by Transmission Electron Microscopy, Cellulose 5 (1998) 201-213.

Supplementary Material

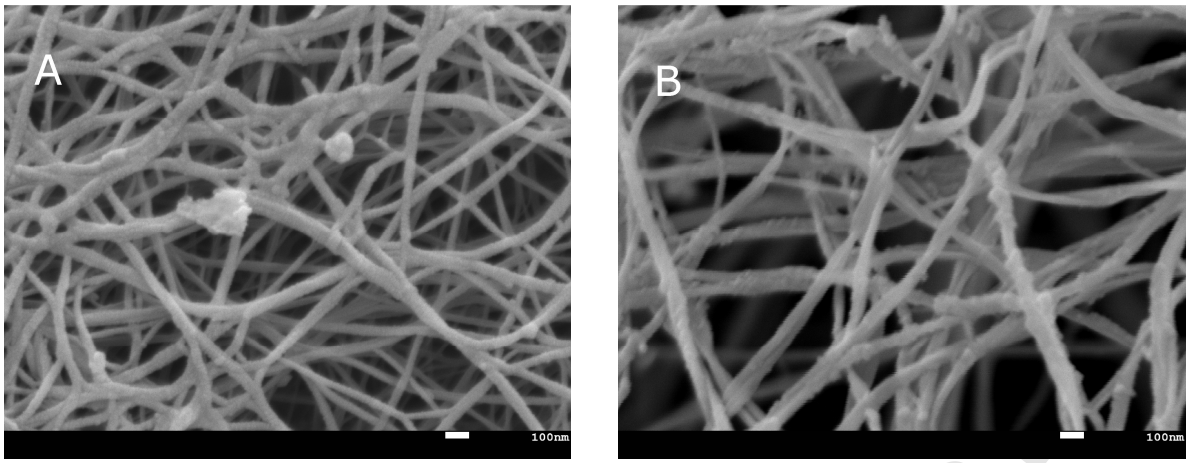

977

979 **Figure S1.** Higher magnification (x50000) FESEM micrographs of freeze-subtituted D-

980 CH-AX (A) and D-CH-MLG (B) showing the presence of nodular structures.